Interpretation of mean free path values derived from off-axis electron holography amplitude measurements

Cathal Cassidy [a,*], Makoto Tokoro Schreiber [a], Marco Beleggia [b,c], Jun Yamasaki [d,e], Hidehito Adaniya [a], Tsumoru Shintake [a]

[a] Okinawa Institute of Science and Technology Graduate University, 1919-1 Tancha, Onna-son, Kunigami-gun, Okinawa 904-0495, Japan
[b] DTU Nanolab, Technical University of Denmark, 2800 Kgs. Lyngby, Denmark
[c] Department of Physics, University of Modena, 41125 Modena, Italy
[d] Research Center for Ultra-High Voltage Electron Microscopy, Osaka University, 7-1, Mihogaoka, Ibaraki, Osaka 567-0047, Japan
[e] Institute of Materials and Systems for Sustainability, Nagoya University, Furo-cho, Chikusa, Nagoya 464-8601, Japan

ARTICLE INFO

ABSTRACT

In this work, we have explored the factors which govern mean free path values obtained from off-axis electron holography measurements. Firstly, we explore the topic from a theoretical perspective, and show that the mean amplitude reconstructed from off-axis holograms is due to the coherent portion of the direct, central object-transmitted beam only – it is not affected by the presence or absence of other scattered beams. Secondly, we present a detailed experimental study which compares mean free path values obtained from hologram sideband, centreband, EELS, and TEM measurements as a function of optical collection angle and energy-loss-filtering. These results confirm that the coherent portion of the direct beam defines the mean amplitude, and additionally show that the coherent portion corresponds to the conventional energy-filtered signal (with threshold 5 eV in this work). Finally, we present summary measurements from a selection of different materials, and compare the results against a simple electron scattering model. This study reinforces the claim that the mean amplitude is defined by the energy-filtered direct beam, and confirms that the contributions of elastic and inelastic scattering to the total mean free path are broadly in line with theoretical expectations for these different materials. These results in aggregate indicate that neither experimental collection angles nor enhanced sensitivity to low-loss phonon scattering affect the mean amplitude signal arising from off-axis holography reconstructions, nor the associated mean free path values which are derived from this mean amplitude.

1. Introduction

In electron microscopy, the mean free path (MFP, λ) is a useful parameter that describes the probability of specific scattering events occurring as the electron beam traverses the specimen (Egerton, 2011). Equivalently, it can be considered as a decay constant describing how the electron wave is attenuated as it travels through the specimen. Ultimately, it embodies the effective thickness of the specimen as seen by the beam electron, and the contrast of the resultant image - for a given accelerating voltage and sample thickness, a material with a short MFP will show high contrast, and vice versa.

However, it is well known that measured MFP values vary with experimental settings, particularly the collection angle. With this in mind, it would be more appropriate to qualify the term MFP with the details of the specific scattering event or experimental detection threshold under consideration. For example, the MFP for scattering events which result in a primary electron energy loss in excess of a certain threshold, the MFP for electron scattering beyond a certain angle, or the MFP between scattering events which cause complete loss of coherence with a specified reference wave, and so on.

MFPs can be derived from off-axis holography amplitude images, and utilized to great effect for quantitative specimen thickness mapping, as shown in the seminal work of McCartney and Gajdardziska-Josifovska (1994). However, the optical configuration and underlying physics is rather different to conventional, intensity-based measurements. In general, experimental measurements of MFP from off-axis holography show quite a lot of variability, and frequently differ from (are shorter than) corresponding measurements utilizing more commonly employed

techniques like EELS (Iakoubovskii et al., 2008; Lubk et al., 2014; Gan et al., 2015; Chung et al., 2007; Pantzer et al., 2014; Cassidy et al., 2017). A tabulation of previously published MFP measurements and calculations for different materials has been published by Kern et al. (2016). To illustrate the point, a brief (non-exhaustive) survey of the literature for silicon MFPs at 200 kV (Pantzer et al., 2014; Chou and Libera, 2003; Twitchett et al., 2003; Cooper, 2016; McCartney et al., 1994), yields holography values ranging from 85 nm to 160 nm. Furthermore, holography values are frequently compared against experimental values and theoretical estimates from EELS, but the relationship between these different techniques is not entirely clear.

For off-axis holography specifically, detailed studies have been conducted on the effect of the collection aperture upon MFP measurements and how this can be related to elastic and inelastic scattering cross-sections (Lubk et al., 2014; Kern et al., 2016). It has also been proposed that, as electron holography is an interferometric technique which depends sensitively upon the coherence of the electrons, that even electrons which have undergone extremely low energy-loss scattering events are rejected from the reconstructed amplitude (Wang, 1993, 2003; Lichte and Lehmann, 2007). Thus, it is proposed that holography may reject many additional electrons (such as phonon-scattered electrons) from the reconstructed amplitude image, which are not rejected from images created via more traditional methods. This could be a plausible explanation for why holography amplitude images show much higher contrast (i.e. shorter mean free paths), than more conventional images or spectroscopy.

While we do not explicitly exclude these effects, we propose that an intrinsic difference in off-axis holography acquisition and data processing, in comparison to standard intensity-based methods, must first be taken into account. In short, we suggest that the holography process of reconstructing a dominant carrier frequency from an interferogram, means that the derived MFP is governed by the coherent portion of the direct, forward-scattered beam, only. We will introduce theoretical arguments and experimental data in support of this statement in the following sections.

The distinctive attributes of holography-based MFP measurements, in contrast to other MFP measurements, were originally observed in our prior investigations on CdTe (Cassidy et al., 2021) and motivated this dedicated study. We have extended the prior work by providing a theoretical explanation of the underlying wave interference and reconstruction phenomena, and further experimental measurements and calculations on different materials.

It is important to mention that MFP measurements are highly susceptible to fluctuations associated with dynamical diffraction effects, as is well known. Only measurements executed on thin, weakly diffracting (amorphous, or off zone-axis crystalline) specimens will yield stable MFP values that may be reliably related to the specimen thickness. This is true for all of the electron beam techniques mentioned in this paper. However, in this work our focus has been to elucidate the unique factors which govern the off-axis holography mean amplitude values, and explain how they differ from other techniques. Thus, while we took care to employ weakly diffracting conditions in our experimental measurements, otherwise we do not explicitly investigate dynamical diffraction effects in this paper. While outside the scope of this current paper, we stress that in general it is a topic of central importance – dynamical diffraction effects must always be carefully considered for reliable and quantitative mean free path and associated thickness measurements.

2. Theory

The ratio of sample thickness t to λ, the "effective thickness", for an electron beam passing through a sample can be measured based on log-ratio methods with the general form

$$\frac{t}{\lambda} = -\ln\left(\frac{I_{obj}}{I_{vac}}\right) \tag{1}$$

where I_{obj} is the measured electron beam intensity averaged over a large uniform sample area and I_{vac} is the intensity through vacuum. The MFP value is thus determined by the intensity lost as a beam travels through a sample of defined thickness. There are various mechanisms by which electrons can be considered to be 'lost' from the object-transmitted intensity signal, depending on the imaging mode and experimental settings being employed. This point is central to the theme of this paper.

2.1. Wave interference

To analyze intensity and holography based images, we must consider the basic electron wave interference in the different microscopy modes being utilized.

For interfering wave pairs of the general form

$$\psi_j = A_j \exp(i(\boldsymbol{k}_j \cdot \boldsymbol{x} + w_j t)) \tag{2}$$

(with wavevectors $\boldsymbol{k}_j$ and angular frequencies ω_j), the associated interference pattern is mathematically described by

$$I_{j,k} = \left|\psi_j + \psi_k\right|^2 = A_j^2 + A_k^2 + 2A_j A_k \cos(\Delta\phi_{j,k}) \tag{3}$$

where $\Delta\phi_{j,k} = (\boldsymbol{k}_j - \boldsymbol{k}_k) \cdot \boldsymbol{x} + (\omega_j - \omega_k)t$. We are not considering any experimental or detection limitations as yet. The first two steady-state terms contribute the mean intensity, while the last (cross) term arises from interference between the waves and contributes oscillating fringes only. If this intensity signal is averaged over a large uniform area, the cross-term will average to zero and will not contribute to the mean intensity value. This can be represented as:

$$\langle I_{j,k}\rangle = A_j^2 + A_k^2 \tag{4}$$

As more waves are considered, each additional wave will contribute a corresponding steady-state term, increasing the mean intensity. By the use of apertures or energy filters, the detected mean intensity can be changed. Therefore, for intensity signal-based MFP measurements such as TEM imaging, changes in the collection angle or energy filtering will directly affect the mean free path measurement. Thus, MFPs determined from TEM intensity measurements are a function of collection angle and energy filtering $\lambda_{TEM} = \lambda_{TEM}(\alpha, \Delta E)$.

For off-axis electron holography, the situation is quite different. We begin the discussion by introducing the vacuum case (without a specimen inserted), allowing the optical configuration and relevant terminology to be introduced, as shown in Fig. 1. In this case, the interference pattern can be represented in the form

$$I_{1,2} = A_1^2 + A_2^2 + 2\mu_{1,2}A_1 A_2 \cos(\Delta\phi_{1,2}) \tag{5}$$

where 1,2 subscripts refer here to vacuum waves in the left and right arms of the interferometer. The first two terms represent the centerband (CB) in the Fourier transform of the hologram while the last term represents the sideband (SB). The SB fringe pattern oscillates at a carrier frequency $\boldsymbol{q}_c$, resulting from the interference of the direct waves which passed on either side of the biprism. $\mu_{1,2}$ is a damping factor, ranging from 0 to 1, and is referred to as the fringe contrast or visibility. It describes purely instrumental factors which reduce the fringe contrast, such as the effect of the finite electron source size (spatial coherence) and energy spread (temporal coherence), as well as mechanical stability and detection efficiency. Eq. (5) has been represented graphically in Fig. 1(b). The central point is that the steady-state (squared) terms define the mean signal, while the interferometric term oscillates about zero and does not directly affect the mean value.

Eq. (5) is entirely valid in vacuum, as it considers the two parallel waves on object and reference arms of the interferometer. However, it is not strictly correct when an object is present, as the object introduces additional scattered beams at different angles and additionally, causes some loss of coherence. Both of these factors must be suitably accounted
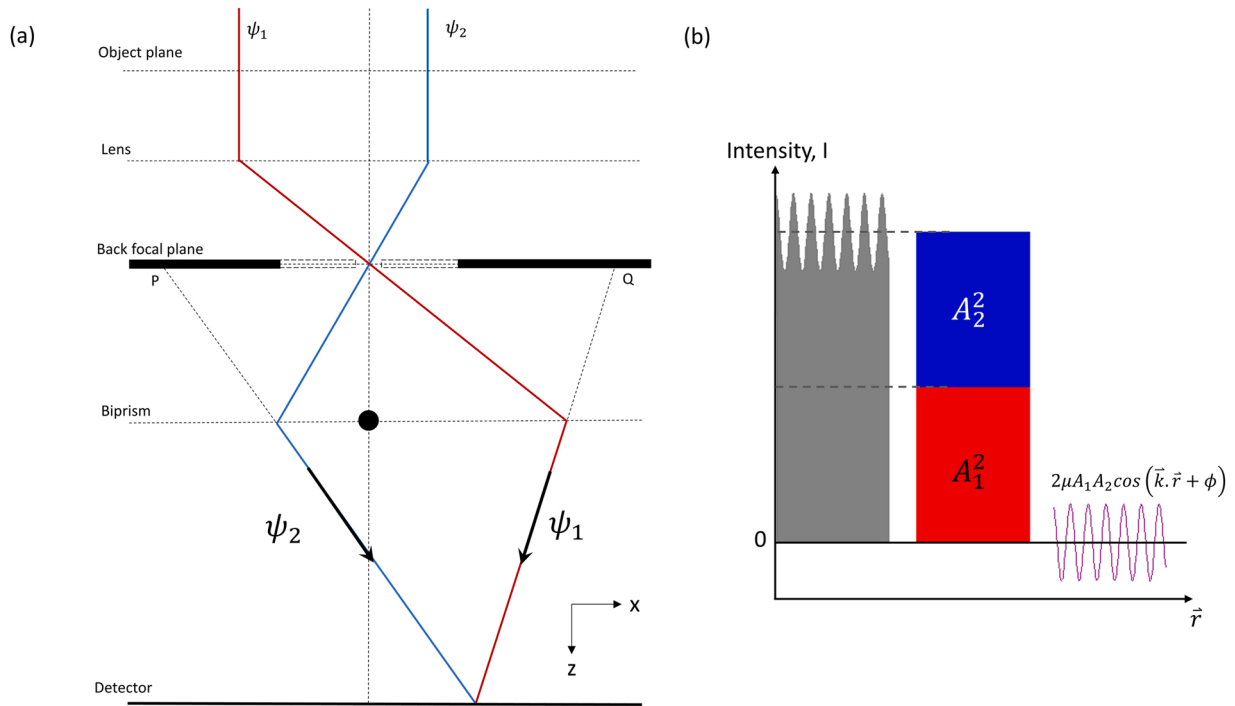
Fig. 1. Introduction to the optical configuration and intensity pattern produced in off-axis holography. This figure depicts the vacuum case, with no specimen inserted into the beam path, and is described mathematically by Eq. (5) in the main text. (a) Ray diagram showing the paths of vacuum waves in the respective arms of the interferometer. Owing to the deflection by the biprism, the different waves appear to originate at different points (P,Q) in the back focal plane. This vacuum case is important in that it introduces the underlying instrumental factors and reference interference pattern, before we proceed to introduce a scattering object into one arm of the interferometer in Fig. 2. (b) The intensity pattern at the detector is composed of steady state (squared) terms, which define the mean intensity signal, and a cross, interference term which oscillates about zero and does not affect the mean intensity, as described in Eq. (5).

for in the mathematical description. The introduction of an object into one arm of the interferometer is shown in Fig. 2. In this case, we refer to the vacuum reference wave as ψ_{vac}, and use the j, k indices for the various object waves. This is the situation depicted in Fig. 2(a). The number of object waves j, k which contribute to the hologram will depend upon the collection angle (aperture) of the microscope, as is apparent in the diffraction patterns shown in Fig. 2(b–c). These diffraction patterns provide a very direct experimental visualization of the constituent waves which are contributing to the hologram.

Considering the beam configuration shown in Fig. 2, the hologram intensity in this case can be written as

$$I_{j,k} = A_{\mathrm{vac}}^2 + \sum_j A_j^2 + \sum_j A_{j(\mathrm{ic})}^2 + \sum_{j \neq k} \mu_{j,k} A_j A_k \cos(\Delta\phi_{j,k})$$
$$+ \sum_j \mu_{\mathrm{vac},j} A_{\mathrm{vac}} A_j \cos(\Delta\phi_{\mathrm{vac},j}) \tag{6}$$

This is a somewhat simplistic representation, but is quite adequate in the context of describing mean amplitudes and intensities, which is the main focus of this work. We will assess the validity of this representation in the Sections 3 and 4.

In Eq. (6), the first four terms represent the centerband (CB) while the last term represents the sideband (SB). Regarding the terminology and definition of coherence in Eq. (6), we treat amplitude terms that contribute to both the centreband and sideband as coherent (and denote by A_j), and those that contribute only to the centreband, as incoherent (and denote by $A_{j(\mathrm{ic})}$). These respective contributions are experimentally well-defined and can be readily extracted from experimental off-axis holograms, by careful inspection of the centreband and sideband signals. We do not yet comment on the physical factors which govern this coherence or incoherence – that will follow later in Sections 3 and 4. Further details on the definitions and underlying assumptions are included in Section S1.

In typical hologram reconstructions, a numerical aperture is placed about the SB (removing all the CB terms) and the carrier frequency q_c is subtracted everywhere to center the SB in Fourier space. As there is a specimen inserted, the dominant carrier frequency signal q_c is created by interference of the vacuum wave ψ_{vac}, and the object direct beam, which we shall specifically designate as ψ_{dir}. The amplitude of the coherent portion of the direct, object transmitted wave is thus denoted A_{dir}. Having isolated the sideband and translated it to the origin in Fourier space, an inverse Fourier transform is then performed to complete the reconstruction. The signal at the origin of the Fourier transform defines the mean of the reconstructed signal, while any other frequencies within the aperture retain an oscillatory character in the reconstructed signal. Averaging over a finite spatial area, the mean intensity of the reconstruction is therefore

$$\langle I_{\mathrm{holo\ recon}} \rangle = \mu_{\mathrm{vac,dir}} A_{\mathrm{vac}} A_{\mathrm{dir}}. \tag{7}$$

where the angle brackets indicate that the intensity is averaged over a uniform area, such that any non-zero frequency terms average to zero. When normalized to the vacuum intensity, the effective thickness from holography SB reconstructions is thus

$$\frac{t}{\lambda_{\mathrm{holo}}} = -2\ln\left(\frac{A_{\mathrm{dir}}}{A_{\mathrm{vac}}}\right) \tag{8}$$

where the factor of two accounts for the presence of amplitude terms rather than intensity. Therefore, the MFP determined through off-axis holography SB reconstructions is only governed by the direct, object-transmitted beam, as described by A_{dir}. Due to this, λ_{holo} is independent of the collection angle used while recording the hologram. Based on our definition introduced in Eq. (6), A_{dir} refers to only that portion of the direct beam which has retained coherence (contributes to centreband and sideband, as observed experimentally). This topic is addressed further in Sections 3 and 4, where the correlation between energy loss
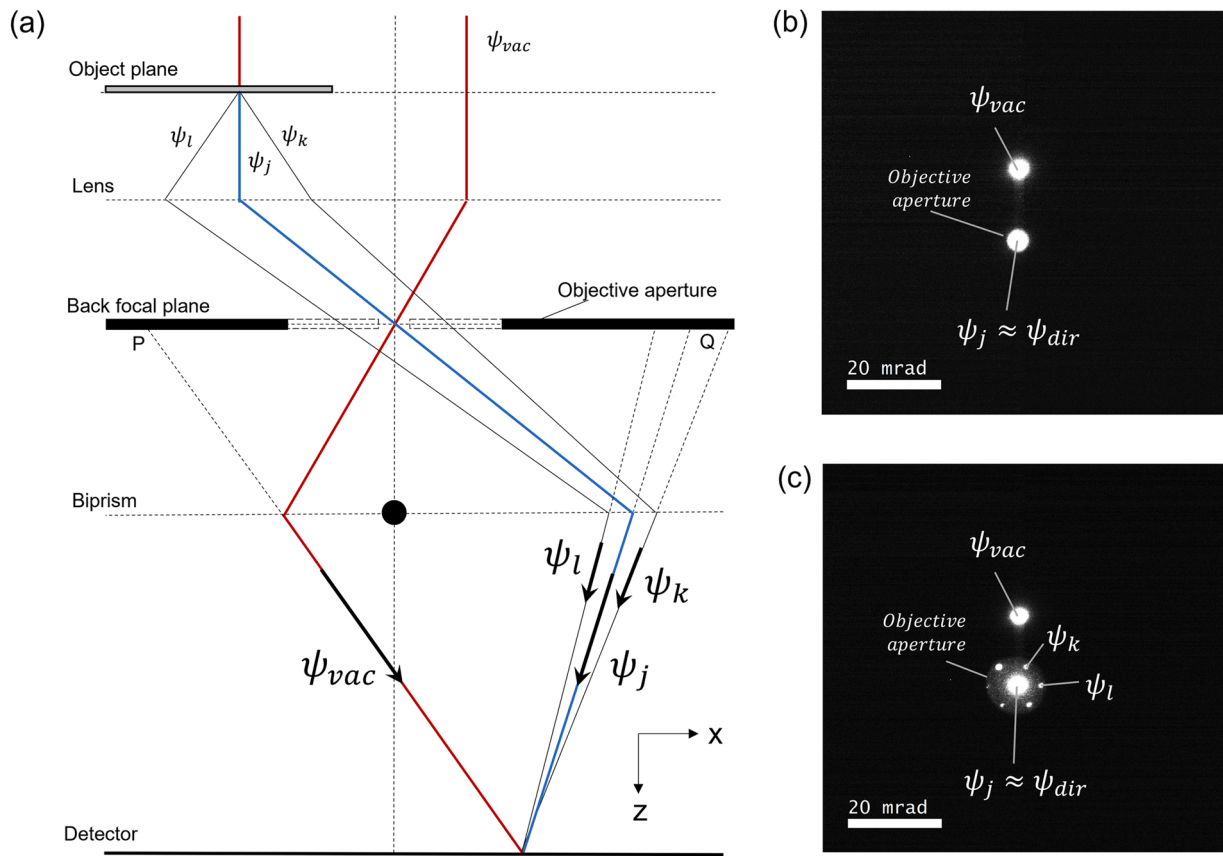
Fig. 2. Hologram formation in terms of interference of multiple discrete waves. (a) Schematic diagram showing the waves which are considered in the accompanying mathematical treatment, particularly Eq. (6). In comparison with Fig. 1, in this case there are now multiple beams in the object arm of the interferometer, arising from scattering with the object, and their quantity can be controlled by choice of objective aperture diameter. (b–c) Experimental diffraction patterns acquired with the specimen, objective aperture and biased electrostatic biprism inserted into the optical path. That the reference and object waves appear to originate at different regions of the back focal plane (P, Q) can be directly visualized. These diffraction patterns provide direct proof that the multibeam formalism described in the main text is genuinely representative of the physical waves propagating in the microscope. In (b), a small aperture has been inserted which allows only the direct beams, in vacuum and object arms, to pass. In (c), a slightly wider aperture has been inserted, allowing some additional diffracted beams to pass. Further information has been included in Fig. S1.

measurements and centreband/sideband amplitude contributions (coherence) will be discussed.

We have included a more detailed version of this whole derivation in the Supplementary information (Section S1, S4). This utilizes a different, more explicit notation and is more cumbersome, but allows a step-by-step look at the full acquisition and reconstruction processes, and explains some of the approximations and assumptions that have been utilized in more detail.

2.2. Mean free path definition in different optical modes

Having introduced the key difference between intensity-based methods, and off-axis holography, there is another factor which must be considered in the computation of mean free paths or effective thickness. The raw output signal type and normalization conventions differ between utilized techniques (such as TEM, EELS, or hologram centreband). If we are to make a quantitative experimental comparison between the results from these different techniques (as we will do in Section 3, Fig. 3 and 4), we must handle this carefully. We summarize our assumptions and definitions below.

For standard (unfiltered) TEM, the effective thickness equation, in terms of mean free path, is as introduced originally in Eq. (1), namely:

$$\left(\frac{t}{\lambda}\right)_{\text{TEM}} = -\ln\left(\frac{I_{\text{obj}}}{I_{\text{vac}}}\right) \tag{9}$$

Next we turn to EELS AND EFTEM. For these techniques, the usual

convention is to normalize the energy-filtered/zero-loss peak signal against the total object transmitted signal (Egerton, 2011). However, to allow consistent comparison, we have instead normalized the signals against the vacuum signal, to be comparable with the vacuum normalized holography results. Specifically, we have used:

$$\left(\frac{t}{\lambda}\right)_{\text{EFTEM}} = -\ln\left(\frac{I_{\text{obj(filtered)}}}{I_{\text{vac}}}\right) \tag{10}$$

$$\left(\frac{t}{\lambda}\right)_{\text{EELS(unfiltered)}} = -\ln\left(\frac{I_{\text{obj(total)}}}{I_{\text{vac}}}\right) \tag{11}$$

$$\left(\frac{t}{\lambda}\right)_{\text{EELS(filtered)}} = -\ln\left(\frac{I_{\text{obj(filtered)}}}{I_{\text{vac}}}\right) \tag{12}$$

For Eqs. (11)–(12), $I_{\text{obj(total)}}$ refers to the total counts, and $I_{\text{obj(filtered)}}$ refers to the zero-loss peak counts, respectively, in the EELS spectrum.

Next we consider the hologram centreband signal. The image is similar to a normal TEM image, and can also be energy filtered, but the presence of the additional background reference wave modifies the contrast and thereby results in slightly different expressions:

$$\left(\frac{t}{\lambda}\right)_{\text{holoCB(unfiltered)}} = -\ln\left(\frac{2I_{\text{obj(unfiltered)}}}{I_{\text{vac}}} - 1\right) \tag{13}$$

$$\left(\frac{t}{\lambda}\right)_{\text{holoCB(filtered)}} = -\ln\left(\frac{2I_{\text{obj(filtered)}}}{I_{\text{vac}}} - 1\right) \tag{14}$$
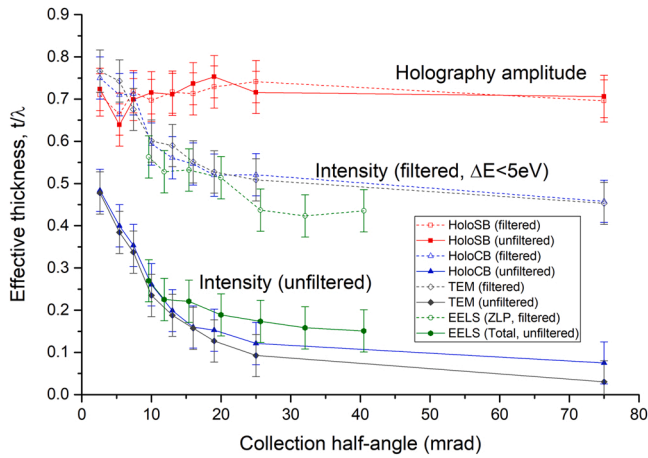
Fig. 3. Variation of measured effective thickness, t/λ, of a local region of an amorphous silicon specimen, as a function of collection angle and energy-filtering ($\Delta E = 0 \pm 5$ eV), for different microscope modes (conventional TEM intensity, off-axis holography centreband, off-axis holography sideband, and EELS). All data was acquired at 300 kV and at room temperature. In the legend, "HoloSB" refers to the amplitude signal reconstructed from the hologram sideband, while "HoloCB" refers to the intensity-based measurement from the hologram centreband. "ZLP" refers to the EELS zero-loss peak, and "Total" refers to the total counts in the EELS spectrum. Slightly different equations were applied to compute the effective thickness for the different modes, as explained in detail in Section 2.2. All signals were normalized using the corresponding vacuum reference value. Note that for the case of EELS, different convergence and collection angles were used, so it is not a direct like-with-like comparison.
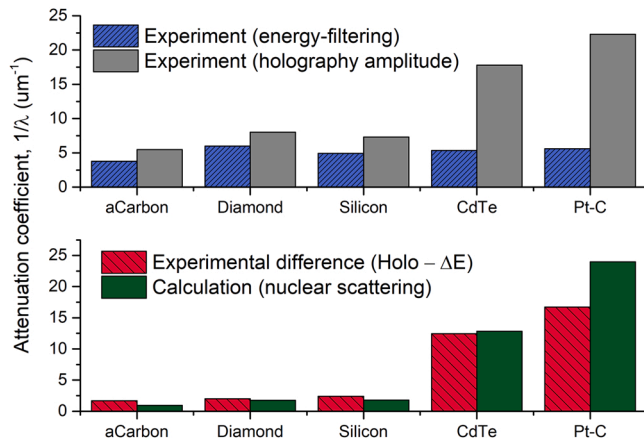
Fig. 4. Experimental measurements and theoretical estimates for attenuation coefficients (reciprocal mean free paths), for a range of materials. All data was acquired at 300 kV and at room temperature, with collection half-angle of 75 mrad. Thickness was estimated based on corresponding phase data. Strongly diffracting conditions were avoided in crystalline materials. (a) Experimental values for attenuation coefficients, based upon energy-filtering (5 eV) and off-axis holography measurements. The difference between energy-filtering and holography values shows a clear trend with the atomic number of the material. We propose that this difference is explained by scattering of electrons, with $\Delta E < 5$ eV, out of the direct beam. (b) Here the difference in attenuation coefficients between holography SB and energy-filtered CB measurements has been explicitly plotted, alongside a calculated value based on the Born approximation for elastic scattering (Eq. (5.30) of Kohl and Reimer, 2008). The material parameters were not well characterized, particularly for amorphous carbon and the Pt-C mixture. For calculations, the amorphous carbon density was estimated as 1.9 g/cm³, and in the absence of composition data, the Pt-C calculation was based on pure Pt. It is not our intention to demonstrate a perfect match, but rather to show that the order of magnitude and qualitative trend are consistent with expectations.

Finally, we consider the hologram sideband, as we derived in Section 2.1. There are two notable features in this case, as already introduced in Eqs. (6)–(8). Firstly, the reconstruction process yields an amplitude, rather than an intensity signal, necessitating an extra factor of two.

$$\left(\frac{t}{\lambda}\right)_{holoSB} = -2\ln\left(\frac{A_{dir}}{A_{vac}}\right) \tag{15}$$

Secondly, only A_{dir}, the coherent portion of the direct beam, contributes to the mean amplitude, as we introduced in Eqs. (6)–(8). In this respect, it is clear that the holography sideband differs substantially from all of the other preceding (intensity-based) techniques. We will quantitatively compare experimental results from each of these techniques in the next section.

3. Results

Having introduced some theoretical background, we proceed to the experimental results. Our goals are twofold. Firstly, we wish to verify that the simple multibeam formalism that we have utilized is valid, and that the mean amplitude signal is indeed defined by the direct beam, only, and is unaffected by the presence of other scattered beams. Secondly, we wish to gain some insight into the underlying physical factors which govern the coherent and incoherent portions, as defined in Eq. (6).

All experiments were performed on a Titan G2 TEM (Thermo Fisher Scientific), operated at 300 kV. The microscope was equipped with a Gatan Quantum 966 energy filter, Gatan UltrascanXP1000 cameras, and a single electrostatic biprism mounted in the selected area plane. The microscope utilized a Schottky XFEG electron source with an intrinsic energy spread of 0.8 eV. For EFTEM work, a slit width of 10 eV centered on the zero-loss peak was employed such that energy losses of > 5 eV were excluded. For holography measurements, we have employed elliptical illumination with long-axis oriented perpendicular to the biprism, to improve the spatial coherence. All measurements were executed in TEM mode. Typical biprism voltages ranged from 140 to 160 V, with fringe contrasts in the range from 8 % to 20 %. All reconstructions were performed using the Holoworks (V5) plug-in for Gatan Digital Micrograph.

3.1. Detailed measurements on silicon

We first performed detailed measurements on a local region of an amorphous silicon specimen, to compare the effective thickness obtained from a range of electron-optical modes. The results are shown in Fig. 3. Comparable data from the same location was acquired in TEM, EELS, and holography (CB and SB) modes, as a function of collection angles and energy filtering. We have also performed similar studies on an amorphous carbon sample (Fig. S2) and crystalline CdTe (Cassidy et al., 2021).

In Fig. 3, we plot the effective thicknesses, t/λ, obtained from the same local region of the sample. These effective thicknesses have been calculated according to the equations shown in Section 2.2. The results are thus directly comparable to each other. A strength of this approach is that the results do not rely upon the accuracy of any parameter measurement (e.g. specimen thickness) or theoretical models.

From Fig. 3, it can be seen that all of the unfiltered intensity-based measurements (unfiltered TEM, holography CB, and EELS (Total)) are very similar to each other. The intensities measured through the sample are high and the effective thicknesses appear small – especially with large collection angles. For the corresponding filtered intensity-based measurements, the effective thickness values are also similar to each other, and appear consistently thicker than the unfiltered measurements as more intensity is removed from the beam. The separation between these filtered and unfiltered measurements is relatively constant as a function of angle as the dominant plasmon-scattering, which is excluded

in the energy filtering case, is strongly forward-peaked.

The SB measurements do not vary with collection angle; which is a strong validation of the theoretical description in Section 2. Furthermore, the SB measurements have no dependence on energy filtering (with threshold at 5 eV). This provides direct evidence that electrons with energy losses greater than 5 eV (plasmon and core scattering) are anyway incoherent – where we use the term in the sense that they add to the holography CB but not the holography SB, as introduced already in the description of Eq. (6).

Interestingly, the effective thickness values from all techniques converge in the limit of energy filtering and small collection angles. Thus, the additional attenuation observed in the off-axis holography amplitude signal, is fully accounted for by the restriction to the central beam, and inelastic scattering (with energy losses in excess of 5 eV). No additional term, arising from low-loss phonon scattering, for example, is necessary. This is discussed further in Section 4.

3.2. Summary measurements on various materials

To build upon the detailed silicon study, we then performed summary measurements on several other materials. Our goal was to confirm the same behavior, and to evaluate the constituent scattering processes which are combining to give the total mean free path in these different materials with different electronic structures and nuclear sizes. We compare these results with a simple electron scattering model.

To consider the summation of several contributing effects to the overall mean free path, it is convenient to utilize the reciprocal mean free path, $1/\lambda$. This is also sometimes referred to as the attenuation coefficient. With this reciprocal notation, the total mean free path can be expressed as a sum of constituent mean free paths for specific scattering events. Results presented in the previous Section 3.1 thus indicate that the total mean free path associated with the off-axis electron holography amplitude signal, $1/\lambda_{\mathrm{holo}}$, can be experimentally decomposed into distinct contributions as

$$\frac{1}{\lambda_{\mathrm{holo}}} = \frac{1}{\lambda_{\alpha > 3\mathrm{mrad}}} + \frac{1}{\lambda_{\Delta E > 5\mathrm{eV}}} \tag{16}$$

This equation is based empirically upon the experimental data shown in Fig. 3. The specific values of 3 mrad and 5 eV in Eq. (15) relate to utilized experimental hardware components, rather than the underlying physical factors. It is presumed that the first term describes what is usually referred to as 'elastic' scattering on the screened nuclear potential, out of the direct beam. It is presumed that the second term describes 'inelastic' scattering events involving an energy loss in excess of 5 eV, involving interactions with plasmons and core electrons in the specimen.

With this in mind, in Fig. 4 we introduce data and calculations from different materials. This comparison of materials and models is a useful exercise, but a caveat is that it also relies upon the accuracy of the parameters (such as thickness, density, composition), as well as the chosen theoretical model for scattering. We must point out that we have not performed very precise material parameter measurements in this work, nor considered sophisticated electron scattering models. Rather, we are primarily interested in the general magnitudes and qualitative trend as opposed to precise values.

In Fig. 4(a), we show the experimentally-derived attenuation coefficients ($1/\lambda$) associated with energy-filtering and off-axis holography sideband measurements, respectively. The energy filtering-derived terms from the different materials have similar magnitudes. The small fluctuations are associated with density and electronic configurations of the associated materials; not with atomic number, as expected. The values are broadly in line with expectations for these materials from EELS literature (Egerton, 2011). The off-axis holography terms, on the other hand, show a significant dependence on material density and atomic number. It is notable that the off-axis holography attenuation coefficients are always larger than the energy-filtering values, and that

the magnitude of the difference scales directly with atomic number. This is consistent with the situation described in Eq. (16). The off-axis holography case appears to be a sum of contributions from inelastic events (which have fairly similar magnitudes across the different materials), and elastic events (which increase dramatically as a function of nuclear size).

In Fig. 4(b), we have explicitly plotted the difference between holography and energy-filtering derived attenuation coefficients, which according to Eq. (16) should yield the elastic, nuclear scattering contribution. Alongside this, we have plotted theoretical estimates for elastic scattering (which depend on atomic number and material density). The theoretical estimates for the various materials were calculated by numerically integrating the Born approximation scattering factor (Eq. (5.30) of Kohl and Reimer, 2008):

$$f(\theta) = \frac{\lambda^2(1 + E/E_0)}{8\pi^2 a_H}(Z - f_x)\frac{1}{sin^2(\theta/2)} \tag{17}$$

where E is the accelerating voltage of the beam electron, a_H is the Bohr radius (0.0529 nm), Z is the atomic number, f_x are the x-ray scattering factors, and θ is the electron scattering angle. The calculation was performed using tabulated x-ray scattering factors from Kirkland (1998) up to the acceptance angle (75 mrad) of the system and multiplying by the atomic density of the material. This simple scattering model is known to perform poorly for high Z elements and in the low angle regime of most importance in this work. Nevertheless, it is informative to see if the general trend is in line with expectations. For the materials considered, the following mass density values were used: silicon 2.33 g/cm^3, amorphous carbon 1.9 g/cm^3, diamond 3.52 g/cm^3, CdTe 5.85 g/cm^3, and Pt 21.45 g/cm^3. The density of amorphous carbon was estimated, and as we did not have information on the specific composition of the Pt-C mixture, we based the calculation on the values for pure Pt.

The results can be seen in Fig. 4(b). These results indicate that the difference between attenuation coefficients derived from energy-filtering and off-axis holography amplitude measurements is broadly consistent with theoretical expectations for elastic scattering out of the direct beam. Pt-C shows a significant discrepancy, but we did use the artificially high values for pure Pt in that calculation, so that is probably not a major concern.

In summary, it seems that for the case of low-density, low Z materials like amorphous carbon, there is actually little difference between energy filtering and holography derived values. For high Z materials like Pt and CdTe, however, there is a dramatic difference between energy-filtering and holography, which can be reasonably approximated by elastic scattering out of the direct beam, on the relatively large nuclei of these materials.

Overall, the results in Figs. 3 and 4 seem to confirm that the mean amplitude signal is defined by the coherent portion of the direct beam, only, and can be reasonably understood in terms of elastic and inelastic scattering events in the material under study.

4. Discussion

In this work, we have utilized a simple multibeam formalism, with coherent and incoherent amplitude contributions, to interpret the mean amplitude signals obtained from standard off-axis holography reconstructions, and correlate them with corresponding electron energy loss measurements. While the treatment is undoubtedly quite simplistic, it does seem to successfully predict the experimental behavior of the off-axis holography mean amplitude signal. In terms of the mean reconstructed amplitude signal, off-axis holography acts as both a scattering-angle filter and an energy-loss filter. According to our understanding, this behavior should hold generally, regardless of the magnification being utilized, the size of the objective aperture, or whether TEM mode or Lorentz mode are being employed. It is also worthwhile to mention that this simple multibeam formalism is valid as we are only considering

the mean intensity signals that are produced, and we ignore the high resolution phase information being transferred via the interference (cross) terms). In general, the conclusions of this paper should be considered to apply to the mean amplitude signal only – we have not yet given careful consideration to the topic of the mean phase.

This work provides some valuable insight into the contribution of very low loss scattering events, such as phonon or thermal-diffuse scattering events, to the measured MFP from off-axis holography. As mentioned in the introduction, it has previously been reported that very low energy-loss electrons, even on the phonon-scale, may be rejected from the reconstructed amplitude, owing to the intrinsically interferometric nature of the technique (Lichte and Lehmann, 2007; Wang, 1993, 2003). Thus, one might expect that an associated extra attenuation component, in comparison to conventional energy-filtering measurements, may be present.

However, our results suggest that this is not directly the case, at least for the experimental conditions that we have utilized. The most important observation is that only the direct object-transmitted beam contributes to the mean amplitude signal, as that is the only object beam which contributes to the signal oscillating at the carrier frequency q_c. As shown in Fig. 3, the attenuation coefficients obtained through holography SB amplitude and conventional intensity-based measurements converge in the limit of small collection angles and plasmon-scale energy filtering. Thus, it would seem that no additional phonon-associated attenuation term is necessary within the central beam. In other words, empirically $A_{dir(ic)}$ is equivalent to $A_{dir(\Delta E > 5\ eV)}$, and conversely, A_{dir} is equivalent to $A_{dir(\Delta E < 5\ eV)}$, referring back to our definitions in Eq. (6). In terms of scattering events at energies below 5 eV, it seems that within the direct beam, either there are few such electrons present, (i.e. phonon-scattered electrons have already been deflected out of the direct beam), or if they are present they retain coherence and contribute to the hologram sideband oscillating at the main carrier frequency q_c. We cannot comment further on the role of phonon-scattered electrons – future measurements with meV-scale monochromated microscopes would be able to directly explore this topic.

It may also be important to mention the intrinsic energy spread of the electron source (0.8 eV in our case), relative to the specimen-related energy losses being considered. This has been discussed in detail previously (Cowley, 1995). Electrons being emitted by the source have some intrinsic variation in their energy, and this is captured via the instrumental μ damping parameter discussed previously (Eq. (5). It may be that the effect of very low-loss events in the specimen (such as phonon scattering events of a few meV) are lost within this intrinsic instrumental spread, and that different behavior might be observed if the electron source were monochromated to below phonon-scale energy levels. If true, $A_{dir(ic)}$ as introduced in Eqs. (6)–(7) may be more fundamentally related to the electrons which experience energy losses greater than energy spread of the electron source $A_{dir(ic)} \equiv A_{\Delta E > \delta E_{source}}$. This is quite speculative, but again further experiments with meV-scale monochromated electron microscopes would be able to directly shed light on this topic.

The results of this work have some implications for thickness mapping, one of the key applications for off-axis holography amplitude mapping (McCartney and Gajdardziska-Josifovska, 1994; Völkl et al., 1999). The results presented here indicate that the mean amplitude signal is dominated by the direct beam only, which should confer insensitivity to the optical collection angle of the utilized microscope hardware. But on the other hand, for crystalline samples this also means that the measurements will be highly sensitive to diffraction effects which redistribute the signal among the direct and diffracted beams. The situation is worse than for conventional intensity based techniques which sum up all of the scattered beams, thereby somewhat smoothing out the effect of the redistributions. Strongly diffracting conditions must be carefully avoided for amplitude measurements and associated thicknesses mapping (as is already well known for phase measurements). This might be a contributing factor in the high degree of variability observed in off-axis holography MFP measurements.

We reiterate that the topic of dynamical diffraction is of utmost importance. Obtaining a stable and easily interpretable mean free path value, and utilizing the mean amplitude as a straightforward measure of specimen thickness, will only be possible for the case of thin, weakly-diffracting specimens. In this work, our focus has rather been to show how the underlying physics and intrinsic content in the off-axis holography signal differs from conventional techniques (under the assumption that weakly diffracting conditions are employed). Thus, the range of thicknesses and diffraction conditions over which reliable thickness mapping can be conducted is beyond the scope of this paper. But clearly, consideration of dynamical diffraction effects is of critical importance in any experimental study of mean free path or specimen thickness.

5. Conclusions

In this work, we have aimed to clarify the interpretation of mean free path values obtained from off-axis electron holography measurements, in comparison to conventional, intensity-based techniques. We have shown that the acquisition and reconstruction process causes the direct object-transmitted beam to define the mean amplitude signal. Practically, this means that the inclusion or exclusion of other scattered beams, governed by the choice of experimental collection angle, has no significant effect on the mean signal. Furthermore, we have shown that electrons which have undergone significant energy losses ($\Delta E > 5$ eV), corresponding to electronic scattering events, are intrinsically excluded from the reconstructed amplitude signal. These results also suggest that the mean free path can be decomposed into contributions from electronic and nuclear scattering terms, in a manner that agrees with basic expectations in terms of electronic structure and atomic number. That MFPs derived from off-axis holography measurements tend to be shorter than those derived from intensity-based energy-filtering techniques, is not caused by smaller collection angles nor intrinsically better energy-filtering. Rather, it is caused by the fact that off-axis holography naturally only reconstructs the mean amplitude signal associated with the central beam. The results presented here may help explain some of the inconsistencies between mean free path values reported in the literature from holographic and conventional intensity/EELS measurements.

Declaration of Competing Interest

The authors declare that they have no known competing financial interests or personal relationships that could have appeared to influence the work reported in this paper.

Data Availability

Data will be made available on request.

Appendix A. Supporting information

Supplementary data associated with this article can be found in the online version at doi:10.1016/j.micron.2022.103346.

References

Cassidy, C., Dhar, A., Shintake, T., 2017. Determination of the mean inner potential of cadmium telluride via electron holography. Appl. Phys. Lett. 110 (16), 163503.

Cassidy, C., Adaniya, H., Shintake, T., 2021. Measurement and analysis of the mean free path governing high-energy electron scattering in CdTe, via off-axis electron holography. J. Appl. Phys. 129 (5), 055109.

Chou, T., Libera, M., 2003. Mean free paths for inelastic electron scattering in silicon and poly (styrene) nanospheres. Ultramicroscopy 94 (1), 31–35.

Chung, S., Smith, D.J., McCartney, M.R., 2007. Determination of the inelastic mean-free-path and mean inner potential for AlAs and GaAs using off-axis electron holography and convergent beam electron diffraction. Microsc. Microanal. 13 (5), 329–335.

Cooper, D., 2016. Off-axis electron holography for the measurement of active dopants in silicon semiconductor devices. J. Phys. D: Appl. Phys. 49 (47), 474001.

Cowley, J., 1995. Chromatic coherence and inelastic scattering in electron holography. Ultramicroscopy 57 (4), 327–331.

Egerton, R.F., 2011. Electron Energy-loss Spectroscopy in the Electron Microscope. Springer Science & Business Media.

Gan, Z., DiNezza, M., Zhang, Y.-H., Smith, D.J., McCartney, M.R., 2015. Determination of mean inner potential and inelastic mean free path of ZnTe using off-axis electron holography and dynamical effects affecting phase determination. Microsc. Microanal. 21 (6), 1406–1412.

Iakoubovskii, K., Mitsuishi, K., Nakayama, Y., Furuya, K., 2008. Mean free path of inelastic electron scattering in elemental solids and oxides using transmission electron microscopy: atomic number dependent oscillatory behavior. Phys. Rev. B 77 (10), 104102.

Kern, F., Wolf, D., Pschera, P., Lubk, A., 2016. Quantitative determination of elastic and inelastic attenuation coefficients by off-axis electron holography. Ultramicroscopy 171, 26–33.

Kirkland, E.J., 1998. Advanced Computing in Electron Microscopy. vol. 12. Springer.

Kohl, H., Reimer, L., 2008. Transmission electron microscopy. Springe Ser. Opt. Sci. 36.

Lichte, H., Lehmann, M., 2007. Electron holography—basics and applications. Rep. Prog. Phys. 71 (1), 016102.

Lubk, A., Wolf, D., Kern, F., Röder, F., Prete, P., Lovergine, N., Lichte, H., 2014. Nanoscale three-dimensional reconstruction of elastic and inelastic mean free path lengths by electron holographic tomography. Appl. Phys. Lett. 105 (17), 173101.

McCartney, M., Gajdardziska-Josifovska, M., 1994. Absolute measurement of normalized thickness, t/λ_i, from off-axis electron holography. Ultramicroscopy 53 (3), 283–289.

McCartney, M., Smith, D.J., Hull, R., Bean, J., Voelkl, E., Frost, B., 1994. Direct observation of potential distribution across Si/Si p-n junctions using off-axis electron holography. Appl. Phys. Lett. 65 (20), 2603–2605.

Pantzer, A., Vakahy, A., Eliyahou, Z., Levi, G., Horvitz, D., Kohn, A., 2014. Dopant mapping in thin FIB prepared silicon samples by off-axis electron holography. Ultramicroscopy 138, 36–45.

Twitchett, A., Dunin-Borkowski, R., Broom, R., Midgley, P., 2003. Quantitative electron holography of biased semiconductor devices. J. Phys.: Condens. Matter 16 (2), S181.

Völkl, E., Allard, L.F., Joy, D.C., 1999. Introduction to Electron Holography. Springer Science & Business Media.

Wang, Z., 1993. Thermal diffuse scattering in high-resolution electron holography. Ultramicroscopy 52 (3–4), 504–511.

Wang, Z.L., 2003. Thermal diffuse scattering in sub-angstrom quantitative electron microscopy—phenomenon, effects and approaches. Micron 34 (3–5), 141–155.